INL/JOU-22-70633-Revision-0

Combined Experimental and Computational Study of Molybdenum and Niobium for Nuclear Sensor Application

May 2022

Ember Sikorski, Richard S Skifton, Lan Li

Changing the World's Energy Future

Idaho National Laboratory

INL/JOU-22-70633-Revision-0

Combined Experimental and Computational Study of Molybdenum and Niobium for Nuclear Sensor Application

Ember Sikorski, Richard S Skifton, Lan Li

May 2022

Idaho National Laboratory
Idaho Falls, Idaho 83415

http://www.inl.gov

Prepared for the
U.S. Department of Energy
Under DOE Idaho Operations Office
Contract DE-AC07-05ID14517

JOM
https://doi.org/10.1007/s11837-022-05317-w

Combined Experimental and Computational Study of Molybdenum and Niobium for Nuclear Sensor Application

EMBER L. SIKORSKI,[1,2] RICHARD S. SKIFTON,[3] and LAN LI [1,2,4]

1.—Micron School of Materials Science and Engineering, Boise State University, Boise, ID 83625, USA. 2.—Center for Advanced Energy Studies, Idaho Falls, ID 83401, USA. 3.—High Temperature Test Laboratory, Idaho National Laboratory, Idaho Falls, ID 83415, USA. 4.—e-mail: lanli@boisestate.edu

Due to their novel electromagnetic and thermal properties, molybdenum (Mo) and niobium (Nb) become optimal temperature sensor materials for nuclear energy applications. We leveraged voltage recorded during a heat ramp to tune a computational method to predict the Seebeck electromotive force (EMF) of Mo and Nb. Using a combined Density Functional Theory (DFT) and Boltzmann Transport Equations (BTE) method the voltage was predicted but did not include the effects of temperature on atomic structure. Combining Ab Initio Molecular Dynamics (AIMD) and BTE included temperature effects on structure optimization and yielded voltages in a good agreement with experiment. Lanthanum (La) and Phosphorus (P) additives in Mo and Nb, respectively, could increase the EMF compared to those of the pure metals. The presence of oxygen (O) in Mo increases the EMF while O in Nb slightly reduces the EMF. Our studies suggested that heat treatment-induced structural changes that lead to a reduction in voltage occur not only at the mesoscale as previously understood but also at the atomic scale.

INTRODUCTION

Molybdenum (Mo) and Niobium (Nb) have long been optimal superconducting materials due to their high critical temperature and magnetic field strength either alone[1,2] or when combined with chalcogenides.[3] Their coupling of electromagnetic behavior with temperature in the form of the Seebeck effect also makes them ideal materials for temperature sensors. In the nuclear energy sector, Mo and Nb can be paired to make thermocouples (TCs) that outperform traditional temperature sensors in research reactors.[4,5] Research reactors allow for testing of accident-tolerant fuel (ATF) materials, towards nuclear energy with even higher safety margins and improved fuel economy.[6,7] Testing ATF materials requires driving them to the temperatures experienced during an accident, allowing for characterization and better understanding of their performance during their namesake scenarios. However, obtaining this characterizing data requires in-pile sensors that can likewise survive under extreme environments.

The temperature sensors composed of Mo and Nb are named high-temperature Irradiation Resistant thermocouples (HTIR-TCs)[4,8–11] and can endure 1000+ h (i.e., 1.2×10^{21} neutrons/cm^2) at 1247°C with no more than 0.6% drift in the temperature reading.[11] At > 1400°C, HTIR-TCs have endured 2000+ h with an estimated drift of 2–3%.[12] Continuing to push the lifetime and performance of the HTIR-TC, we seek to better understand possible causes of reduced TC performance.

TC performance is controlled by the Seebeck coefficient of each of the TC thermoelements, as shown in Fig. 1. Utilizing the Seebeck effect, TCs consist of two dissimilar metals connected at a junction. The temperature difference between the hot junction, where temperature is measured in a reactor, and the cold junction, the reference temperature measured outside of the reactor, will produce a proportional voltage difference between the two metals. Once the respective voltage changes are fitted to the desired temperature range, the TC

(Received January 18, 2022; accepted April 18, 2022)

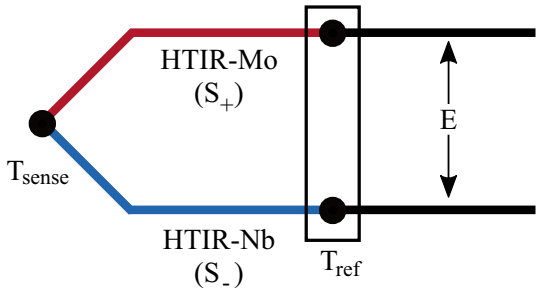

Fig. 1. Schematic of a HTIR-TC consisting of two thermoelements: HTIR-Mo and HTIR-Nb which act as the positive and negative thermoelement, respectively. Each thermoelement has its own respective Seebeck coefficient, S. One end of the TC is placed into a reactor to measure temperature, T_{sense}, while the other end is held at a constant temperature, T_{ref}, outside of the reactor. Due to the Seebeck effect, the TC produces a voltage, E, proportional to the temperature difference, T_{sense}–T_{ref}.

can be used to monitor temperature. Mathematically, this Seebeck electromotive force (EMF), E, can be determined by taking the integral of the difference of the Seebeck coefficients for each thermoelement:

$$E = \int_{T_{ref}}^{T_{sense}} (S_+ - S_-)dT, \quad (1)$$

where T_{sense} is the sensing temperature and T_{ref} is the reference temperature. In a HTIR-TC, the positive Seebeck coefficient, S_+, corresponds to HTIR-Mo and the negative Seebeck coefficient, S_-, corresponds to the HTIR-Nb. The Seebeck coefficient is intrinsically controlled by the atomic structure-electronic property relationships of the materials. Given the extreme environment the HTIR-TC is designed for, it is susceptible to structural changes due to temperature, radiation-induced defects, and/or transmutation. These structural changes will affect the Seebeck coefficients of the HTIR thermoelements, resulting in changes in the HTIR-TC performance. By better understanding the structure-property relationships of the thermoelements, we can identify the material factors that enhance and detract from in-pile HTIR-TC performance.

Mo and Nb were selected as the two HTIR thermoelements because of their balance of high temperature and irradiation resistance compared with traditional TC thermoelement materials, such as platinum (Pt), rhodium (Rh), and nickel (Ni) alloys.[5] Mo and Nb have thermal nuclear cross sections of 2.65 and 1.15 barns and melting temperatures of 2610°C and 2470°C, respectively.[4] In contrast, Type B (Pt-30%Rh/Pt-6%Rh) TCs, which are rated for temperatures up to 1820°C, consist of Pt and Rh with thermal cross sections of 10 and 150 barns, respectively. With a large thermal cross section, 6 wt.% of Rh is expected to transmute during an 800-day irradiation in a pressurized water reactor.[13] TCs composed of Ni alloys, Type K (Chromel/Alumel) and Type N (Nicrosil/Nisil), though less susceptible to irradiation, degrade at temperatures > 1000°C.[4,5,14] In addition, doping and alloying can further tune Mo for optimal in-pile TC performance. Mo wire doped with Lanthanum Oxide (La_2O_3) has yielded the highest temperature resolution, or V/°C, allowing for smaller changes in temperature to be reflected in the TC reading.[9]

Since the HTIR-TC performance depends on both the atomic and electronic structures of the thermoelements, we leveraged atomistic modeling methods to better understand the controlling factors. In this work, we combined experimental and computational methods to study the effects of heat treatment and thermoelement composition on the HTIR-TC voltage. We investigated the HTIR-Mo and HTIR-Nb thermoelements individually using real-time voltage measurements during heat treatment in a tube furnace, Density Functional Theory (DFT), Boltzmann Transport Equations (BTE), and Ab initio Molecular Dynamics (AIMD). First, we examined the effect of heat treatment experimentally on the voltage of each HTIR-thermoelement. Second, through comparing the experimental voltage with the voltage predicted from DFT and BTE, we could determine the atomic structure-performance relationships of HTIR thermoelements. Third, we applied AIMD and BTE to determine the temperature effect on the atomic structures and performance of the HTIR thermoelements.

METHODS

Experimental Methods

Two TCs were fabricated by coupling (1) HTIR-Mo with Pt and (2) HTIR-Nb with Pt. Heat treatment and voltage recording details have been described previously.[10,11] In summary, each thermocouple was placed in a tube furnace opposite a Type B TC, suitable for high temperatures but not irradiation, for temperature measurement. The TCs were heated to 1600°C at a rate of 5°C/min. The furnace was held at 1600°C for 72+ h. The furnace was cooled to room temperature at 5°C/min. The HTIR-Mo thermoelement contains 0.5 – 1 wt.% La_2O_3, and the HTIR-Nb thermoelement contains 496 and 424 μg/g of Phosphorus (P) and Oxygen (O), respectively.

Computational Methods

DFT calculations were performed using the Vienna Ab initio Simulation Package (VASP).[15] Spin-polarized generalized gradient (GGA) exchange-correlation functions were used following the Perdew Burke Ernzerhoff (PBE) formulation.[16] Plane-wave basis sets were implemented utilizing projector-augmented wave (PAW) pseudopotentials. Simulations were performed with a cutoff energy of 550 eV and a minimum of 5 × 5 × 5 gamma-

Journal : 11837_JOM Dispatch : 28-4-2022 Pages : 10
Article No.: 5317 ☐ LE ☑ CP ☐ TYPESET ☑ DISK

centered k-points. The Hubbard +U term[17] was applied to Mo and Nb atoms during electronic structure calculations to improve the DFT description of d electrons. Effective U-terms of 8.6 and 4.0 eV were applied to Mo[18] and Nb,[19] respectively. The Boltzmann transport equations were solved using BoltzTraP2.[20] Atomic structures were visualized using Visualization for Electronic and Structural Analysis (VESTA).[21]

In this article, we will use "DFT" and "AIMD" to distinguish between VASP calculations performed *without* and *with* temperature, respectively. For DFT calculations, the pure Mo and Nb metals were modeled using their body center cubic (BCC) unit cell (Fig. 2a and d) with experimental lattice constants of 3.146 and 3.311 Å, respectively.[22,23] The Mo unit cell was then supersized to the 4×4×4 supercell with one atom replaced by La to approximate a concentration of 1.13 wt.% La (Fig. 2b). Similarly, the Nb unit cell was then supersized to the 4×4×4 supercell with one atom replaced by P to approximate a concentration of 0.26 wt.% P (Fig. 2e).

For AIMD calculations, simulations were performed using an NVT ensemble with a 220 eV cutoff energy and sampled at the gamma point with 0.25-fs timesteps. Temperature was controlled with the Nosé-Hoover thermostat, and the Nosé mass was set to correspond to 40 time steps.[24] To balance between computational cost and accuracy, the cutoff energy of 220 eV, higher than default the minimum cutoff energies for both Mo and Nb elements, was selected. Our test calculations with 0.25 fs timesteps and 220 eV cutoff energy agreed well with the experimental voltage measurement. Convergence tests showed that the 220 eV-cutoff structure was converged compared with the equivalent equilibration AIMD run at 550 eV as shown in Fig. 3. In each system an additional metal atom was replaced with O, resulting in Mo 1.13 wt.% La 0.13 wt.% O (Fig. 2c) and Nb 0.26 wt.% P 0.14 wt.% O (Fig. 2f). Electronic structures used for the Seebeck coefficient calculations were obtained for the AIMD-relaxed structures using a 320 eV cutoff energy, 5 × 5 × 5 gamma-centered k-points, and Hubbard +U terms of 8.6 and 4.0 eV for Mo and Nb, respectively.

RESULTS AND DISCUSSION

Experimental Voltage Measurement

For in-pile use, the HTIR-TCs are constructed in their now standard HTIR-Mo coupled with HTIR-Nb build. However, the combined voltage of a HTIR-TC is difficult to compare with the absolute, thermoelement-specific voltages obtained through modeling. For this reason, we fabricated two special HTIR-TCs where each individual HTIR-thermoelement was coupled with a Pt thermoelement. As the absolute Seebeck voltage of Pt is known experimentally,[25] its contribution can be removed to yield the absolute EMF of both HTIR-Mo and HTIR-Nb thermoelements.[11] The results of the experimental

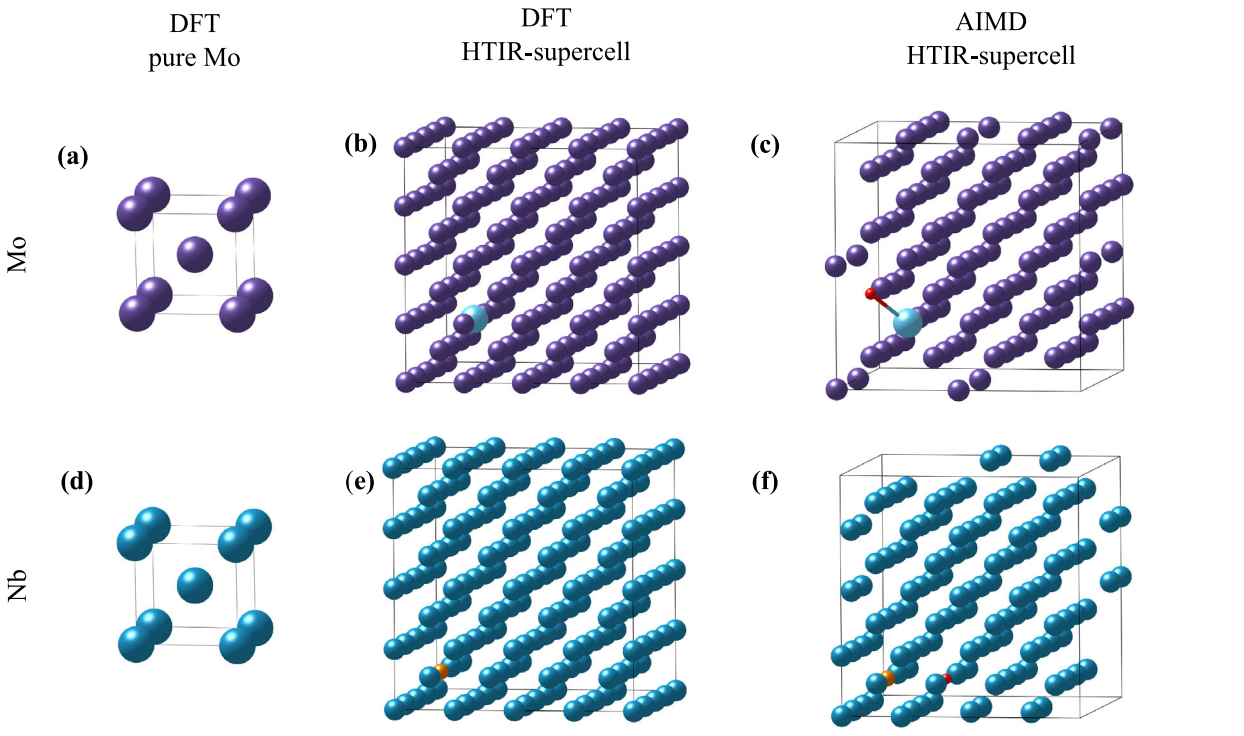

Fig. 2. Starting atomic structures for (a) pure Mo, (b) the HTIR-Mo supercell used in DFT, (c) the HTIR-Mo supercell used in AIMD, (d) pure Nb, (e) the HTIR-Nb supercell used in DFT, and (f) the HTIR-Nb supercell used in AIMD. Purple, blue, light blue, orange, and red atoms represent Mo, Nb, La, P, and O, respectively.

Journal : 11837_JOM Dispatch : 28-4-2022 Pages : 10
Article No.: 5317 ☐ LE ☑ CP ☐ TYPESET ☑ DISK

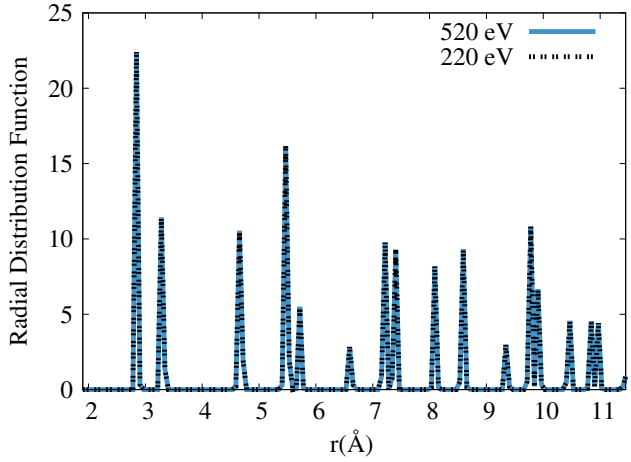

Fig. 3. Radial distribution function in Å of HTIR-Nb AIMD equilibration at 20°C using 220 eV and 520 eV cutoff energies.

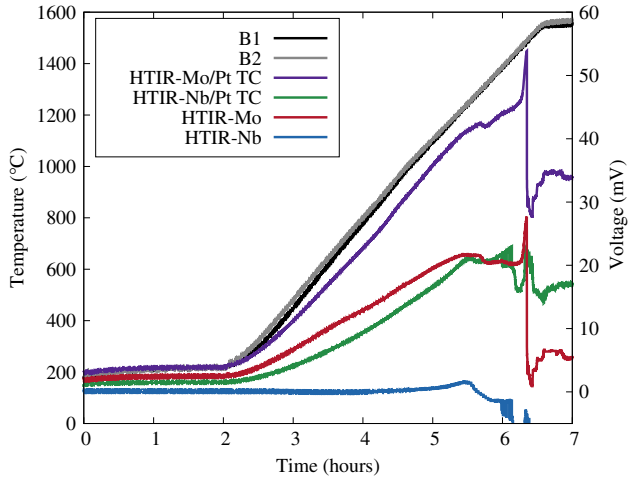

Fig. 4. Experimental temperature profile as measured by two Type B TCs, voltage output by the HTIR-Nb – Pt and HTIR-Mo – Pt TCs during the heat treatment, and voltage output by the HTIR-Nb and HTIR-Mo thermoelements during the heat treatment. The heat soak at 1600°C begins just after 6.5 h.

heat treatment and voltage measurements are shown in Fig. 4. The two Type B TCs (B1 and B2) were placed opposite the special HTIR-Mo/Pt and HTIR-Nb/Pt TCs in the tube furnace. During the heat ramp, the Type B TCs were used to read the temperature while the voltages of the special HTIR-TCs were recorded. Combining these readings allowed the voltage to be plotted vs. temperature to compare to modeling. The HTIR-Mo and HTIR-Nb curves in Fig. 4 show the absolute EMF of the respective thermoelements obtained by subtracting the Pt contribution from the special HTIR-TC voltage readings.

Both the HTIR-Mo and HTIR-Nb show variations in the EMF as the temperature approaches 1600°C and begins the annealing process. These EMF fluctuations have previously been attributed to grain growth.[9] HTIR-TCs destined for use in research reactors undergo standardized heat treatments to stabilize the grain growth before they are calibrated.[10,11] Following the fifth order polynomial fitting of EMF reported previously for calibrated HTIR-TCs,[11] the polynomial coefficients of the HTIR-Mo and HTIR-Nb thermoelements are provided in Table I. The fit is taken from the beginning of the heat treatment (200°C) up to approximately 1200°C before the EMF variations begin. To better understand the compositional and atomic structure effects on the experimental measurements, we applied a combination of DFT, BTE, and AIMD methods to provide insights into the Seebeck coefficient of each thermoelement.

Table I. Polynomial coefficients of EMF as a function of temperature for HTIR-Mo and HTIR-Nb thermoelements from 200 to 1200°C following $E(T) = AT^5+BT^4+CT^3+DT^2+ET+F$

Coefficient	HTIR-Mo	HTIR-Nb
A	−4.687 E−14	1.416 E−14
B	1.713 E−10	−4.484 E−11
C	−2.389 E−07	5.584 E−08
D	1.605 E−04	−3.240 E−05
E	−3.300 E−02	8.118 E−03
F	4.120 E+00	−6.085 E−01

DFT Calculations

To verify the accuracy of DFT and BTE to predict Seebeck coefficients, we started with pure Mo and pure Nb materials (Fig. 2a and d). Figure 5 shows the calculated Seebeck coefficients as a function of temperature, which generally agrees with the experimental values for both pure Mo[26] and pure Nb.[27] We then extended the models to the supercells containing La and P, as shown in Fig. 2b and e, representing HTIR-Mo and HTIR-Nb, respectively. The resultant Seebeck coefficients were integrated with respect to temperature as in Eq. 1 to obtain the voltage for each thermoelement. Figure 6 shows the calculated voltages for the HTIR and pure metals compared with the experimental values from Experimental Voltage Measurement Experimental Voltage Measurement.

With the addition of La in Mo, the voltage predicted by DFT-BTE is increased for most of the temperature range compared to pure Mo (Fig. 6a). This voltage increase is in agreement with experimental results demonstrating the high temperature resolution of Mo with a La_2O_3 dopant.[9] The effect of P on Nb temperature resolution has not previously been reported but is likewise shown here to greatly increase the voltage compared to pure Nb (Fig. 6b). These results demonstrate a close relationship between atomic structure and Seebeck EMF.

In Fig. 6a, there is a reasonable agreement between the DFT calculated and experimental

HTIR-Mo voltages from 200 to about 600°C. However, the more parabolic nature of the calculated HTIR-Mo voltage becomes apparent above 600°C as it diverges from that of experiment. For HTIR-Nb, the calculated voltage starts off close to the experimental voltage at 200°C but diverges as the temperature increases (Fig. 6b). To understand the implications of these results, we need to examine the assumptions utilized in the DFT-BTE method along with the supercells. First, the atomic structure obtained from DFT was used for the full temperature integration range in the BTE. This assumed that the atomic structure remained the same and no structural distortion would occur at all temperatures, which might be an inaccurate representation, especially at higher temperatures. Second, O was not included in the DFT supercells and as such the DFT voltages in Fig. 6 do not include any contribution from O.

According to Fig. 6 and DFT assumptions, we can propose four predictions about the HTIR thermoelements. The variation between the calculated and experimental HTIR-Mo voltage suggests (1) HTIR-Mo undergoes structural changes at or above 600°C and/or (2) O affects the trend of the voltage produced by the HTIR-Mo thermoelement. In HTIR-Nb, the addition of P increases the magnitude of the pure Nb voltage to greater than the experimental voltage. This suggests a competing factor(s), which counteracts the voltage increase from P, ultimately reducing the HTIR-Nb voltage to nearly zero. The competing factor(s) could be (3) structural changes with respect to temperature and/or (4) O content. To further validate these predictions, we studied both the HTIR-Mo and the HTIR-Nb systems with consideration of the temperature effect using AIMD.

To determine the initial position of O for AIMD calculations, we performed DFT calculations of O at various metal substitutional positions with respect to the La or P additive in the HTIR supercells. Substitutional sites were considered because of strong favorable interaction energy between O and vacancies in BCC metals.[28] The incorporation energy, E_{inc}, for O at each site was calculated using the following equation:

$$E_{inc} = E_{nM+A+O} - \left(E_{(n+1)M+A} - E_M\right) - \frac{1}{2}E_{O_2}, \quad (2)$$

where E_{nM+A+O} is the energy of the supercell with n metal atoms containing either the P or La additive and O at substitutional metal sites, $E_{(n+1)M+A}$ is the energy of the metal supercell with only a P or La additive at a substitutional metal site, E_M is the energy of a single metal atom in the pure metal unit cell, and E_{O_2} is the energy of a single O_2 molecule. Greater magnitude in a positive incorporation energy value indicates more energy required for O to enter the site. Conversely, greater magnitude in a negative incorporation energy value indicates a more favorable exothermic process to place O at the substitutional site. We considered the first nearest neighbor site, the second nearest neighbor site, and a site located far from the P or La additive as substitutional locations for O. As shown in Table II, O can exothermically enter any of the substitutional Nb sites. However, energy is required to place O in Mo at the far or second nearest

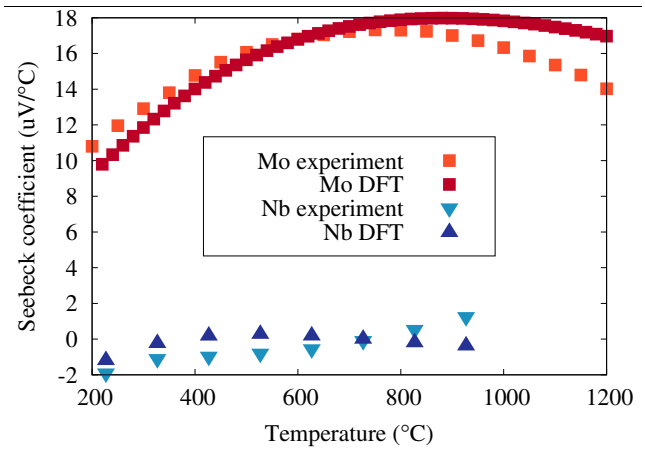

Fig. 5. Comparison of Seebeck coefficients for pure Mo and Nb from experiment[26,27] and computation.

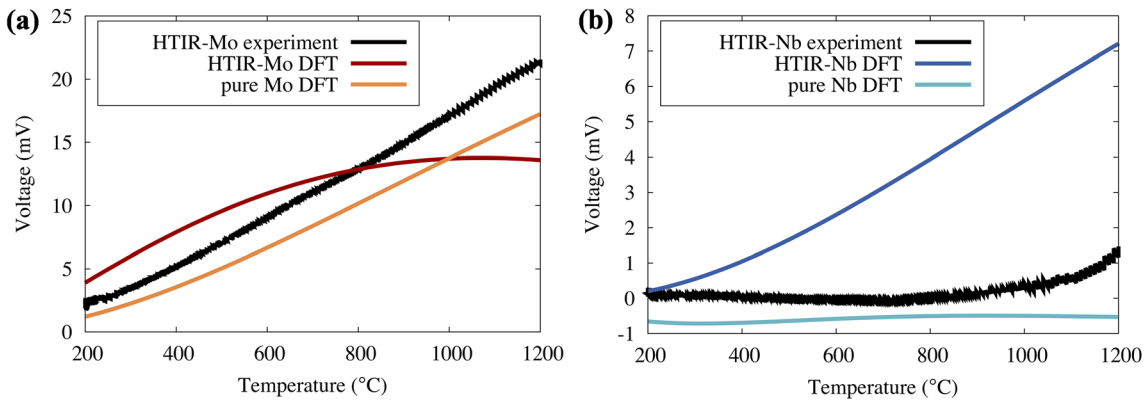

Fig. 6. Comparison of the voltages obtained from experiment and DFT for (a) Mo and (b) Nb. The HTIR-Mo DFT structure contains 1.13 wt.% La and the HTIR-Nb DFT structure contains 0.26 wt.% P.

Journal : 11837_JOM Dispatch : 28-4-2022 Pages : 10
Article No.: 5317 ☐ LE ☑ CP ☐ TYPESET ☑ DISK

Table II. Incorporation energies of O in Nb and Mo when substituting a metal atom far from, at the 1st nearest neighbor, or at the 2nd nearest neighbor site relative to the HTIR additive P or La, respectively

O position	Incorporation energy (eV)
Nb system	
Far	−0.50
1st nearest neighbor	−0.96
2nd nearest Neighbor	−1.34
Mo system	
Far	0.65
1st nearest neighbor	−0.14
2nd nearest neighbor	0.26

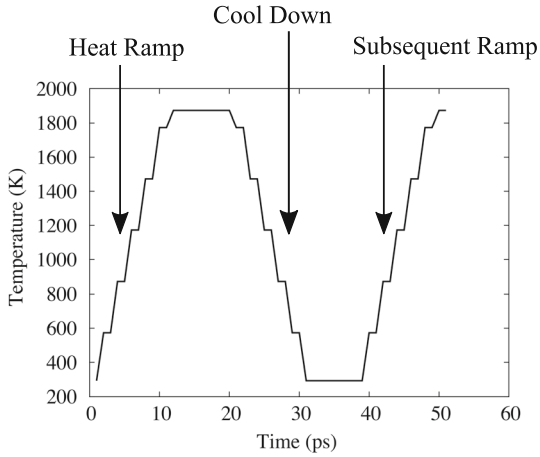

Fig. 7. Temperature profile of the AIMD heat treatment performed on the HTIR-Mo and HTIR-Nb structures

neighbor position. Only the first nearest neighbor position is exothermically favorable for O in Mo. The most favorable site for O in Nb is the second nearest neighbor with respect to the P atom while the most favorable site in Mo is the first nearest neighbor with respect to the La atom. We then started with these most favorable sites for the O atom in the AIMD calculations, as shown in Fig. 2c and f.

Ab-Initio Molecular Dynamic Simulations

Using AIMD allowed us to not only include the effect of temperature on atomic structure but also follow specific heating and cooling profiles. By also including O in the AIMD simulations, we could evaluate the four predictions outlined in DFT Calculations section. Experimentally, heat treatment is performed on HTIR-TCs before calibration to reduce drift upon a subsequent insertion into a high-temperature experiment.[10] Mirroring experimental heat treatment, the AIMD simulations followed the process including the ramp to 1600°C, the hold at 1600°C, and the cool down to room temperature. A subsequent ramp was performed to investigate how the treatment stabilized the structure such that subsequent insertion into a reactor would yield less drift than it would without heat treatment. The full temperature profile performed using AIMD is shown in Fig. 7.

Using the DFT-BTE method temperature was incorporated only once during the integration of the Seebeck coefficients. Using the AIMD-BTE method temperature was incorporated twice: first during the simulation of the atomic structure and second during the integration of the Seebeck coefficients. While DFT was performed at 0K, AIMD ran with given temperature. By using the structures obtained from AIMD as input for BTE, the effect of temperature on atomic structure was included in the calculation of voltage. As shown in Fig. 8, we can extrapolate each AIMD atomic structure over the full temperature range, like the DFT-BTE method shown in Fig. 6. Computational results are shown against the voltage measured during the experimental heat ramp.

With the inclusion of O and temperature effects on the structure, the HTIR-Mo AIMD 20°C voltage increases to 25 mV at 1200°C (Fig. 8a), compared to the HTIR-Mo DFT voltage which plateaus at almost 14 mV. As the AIMD temperature increases, the HTIR-Mo EMF at 1200°C is calculated as 28.1, 21.0, 18.43, and 27.5 mV for the 300, 600, 900, and 1200°C atomic structures, respectively. Experimentally, the HTIR-Mo voltage is 21.37 mV at 1200°C. The 600°C atomic structure gives the closest overall voltage to that measured by experiment.

Like HTIR-Mo, the HTIR-Nb AIMD 20°C voltage is the first look at the effects of adding both temperature and O to the AIMD model (Fig 8b). The AIMD 20°C voltage is slightly lower than the DFT-BTE curve, yielding voltages of 6.29 and 7.21 mV, respectively, at 1200°C. As the AIMD temperature increases, the HTIR-Nb EMF at 1200°C is calculated as 3.65, 0.93, −1.59, and 0.39 mV for the 300, 600, 900, and 1200°C atomic structures, respectively. Experimentally, the HTIR-Nb voltage is 1.17 mV at 1200°C. Like HTIR-Mo, the 600°C atomic structure gives the closest overall voltage to that measured by experiment. As the atomic composition remains constant throughout the heat ramp, the AIMD voltages provide insight into the structural changes with respect to temperature. While DFT overestimates the HTIR-Nb voltage, AIMD demonstrates that structural changes lead to a reduction in the voltage, agreeing better with experiment.

To quantify the structural changes, radial distribution functions (RDFs) (Fig. 9) were obtained for the HTIR thermoelements from DFT and from the AIMD heat-up/cool-down cycles in Fig. 7. The first peak in an RDF indicates the average distance between each particle and its first nearest neighbor, and so on. The higher and narrower the peak is, the more particles that have a neighbor at the given

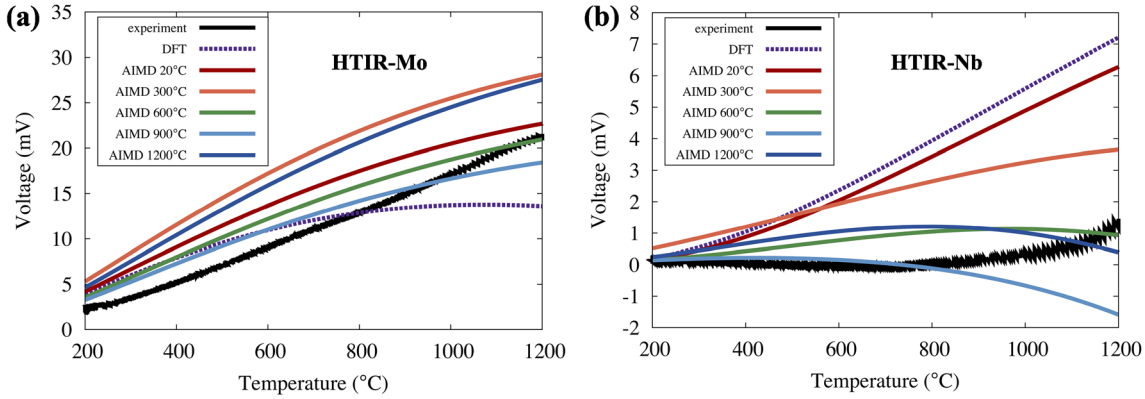

Fig. 8. Voltage produced by (a) HTIR-Mo and (b) HTIR-Nb as measured in experiment, calculated in DFT, and calculated in AIMD. For the AIMD voltages, Seebeck coefficients obtained from an atomic structure at the given temperature were integrated over the full temperature range. For HTIR-Mo, the DFT structure contains 1.13 wt.% La and the AIMD structures contain 1.13 wt.% La 0.13 wt.% O. For HTIR-Nb, the DFT structure contains 0.26 wt.% P and the AIMD structures contain 0.26 wt.% P 0.14 wt.% O.

distance. The broader the peak is, the more this distance varies from atom to atom. In Fig. 9a and b, the AIMD 20°C RDFs are identical to the DFT RDFs for both HTIR-Mo and -Nb. This informs that while both temperature treatment and O are added during the transition from DFT to AIMD methodology, the only factor contributing to the differences between the DFT voltages and the AIMD 20C voltages (Fig. 8) is the O content.

Heating the HTIR thermoelement systems induces disorder in the structures. In Fig. 9c–f, the RDFs at 20°C consist of clearly defined peaks, indicating the crystalline structure expected in the metals. However, starting at 300°C the peaks broaden as the temperature increases, indicating a decrease in order. In both the HTIR-Mo and -Nb structures during the heat ramp, peak 5 becomes a shoulder of peak 4, peak 6 and 11 nearly disappear, peaks 7 and 8 merge, and peaks 15 and 16 merge. At 1600°C in HTIR-Nb, there are nonzero values between each of the original peaks. This noise is not present to the same extent in the HTIR-Mo system. In HTIR-Nb the noise is so great that original peaks 6 and 11 could easily be mistaken for noise. HTIR-Nb exhibits further disorder as original peaks 9 and 10 as well as peaks 14 through 16 merge at 1600°C. Conversely, in HTIR-Mo peaks 9, 10, and 14 retain definition even though the counts are greatly reduced.

During the cool down shown in Fig. 9g–h, nearest neighbor counts begin to return to each of the peaks. The original peaks 4 and 5, peaks 7 and 8, peaks 12 and 13, and peaks 15 and 16 remain merged in both structures even after they return to room temperature. The intensity of the peaks at 20°C after the cool down is significantly reduced compared to the 20°C peaks before the heat ramp. As can be seen during the subsequent ramp in Fig. 9i and j, this reduces the variation in the peaks between temperatures. Consequently, we can interpret this as less structural change occurring during the subsequent ramp correlating to less drift in the TC measurement. Experimentally, the heat treatment stabilizes the HTIR thermoelement structures by preemptively causing structural changes. In this way, temperature-induced structural changes are included in the TC calibration instead of causing drift in in-pile performance.

DISCUSSION

In DFT Calculations section, we outline four predictions about the structural and compositional effects on the voltage produced by each thermoelement. According to the AIMD RDF (Fig. 9c and e), the HTIR-Mo structure becomes more disordered as the temperature increases. The 600°C step exhibits the first complete merge of peaks 7 and 8. The number of peaks and peak intensities remain relatively constant after 600°C in agreement with prediction (1). In prediction (2), we hypothesize that O changes the trend of the HTIR-Mo voltage. As shown by the RDFs in Fig. 9a, the DFT and AIMD 20°C structures are identical. This indicates that while temperature treatment and O are added during the transition from DFT to AIMD methodology, the only factor contributing to the difference between the HTIR-Mo DFT voltages and AIMD 20°C voltages is the O content. As such, Fig. 8a shows that O reduces the parabolic curvature of the voltage. The effect of O on the HTIR-Mo EMF becomes more pronounced with increasing temperature, i.e., the DFT and AIMD 20°C EMFs are < 0.3 mV apart at 200°C, but this gap increases to 8.3 mV by 1200°C. It confirms that O changes the HTIR-Mo voltage trend in agreement with prediction (2).

In prediction (3) we hypothesize that temperature-dependent structural changes cancel out the voltage increase due to *P*. The HTIR-Nb RDFs (Fig. 9d and f) show significant structural changes as temperature increases, with nonzero values between peaks and the merging of even more peaks than in HTIR-Mo. In prediction (4), we hypothesize

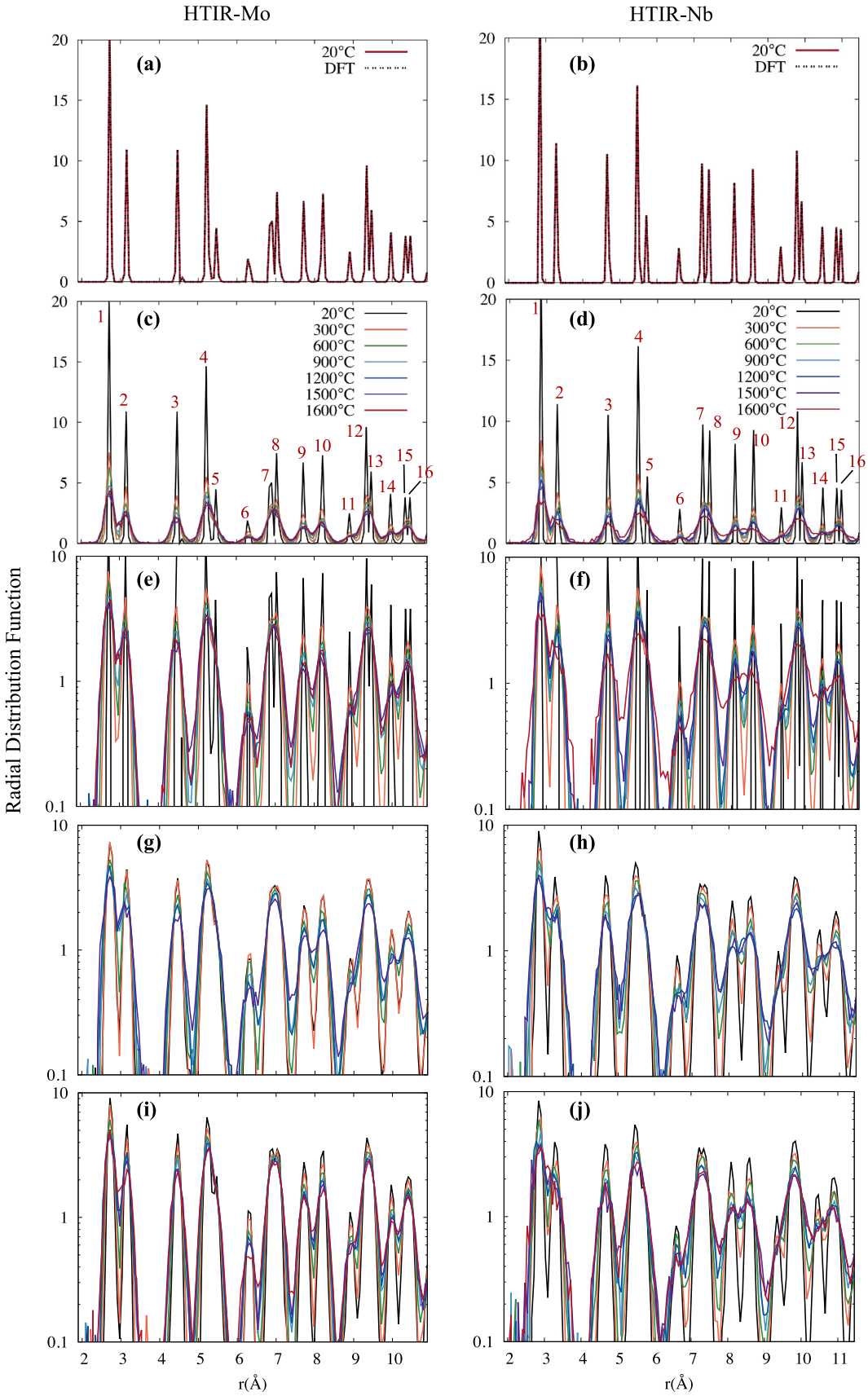

Journal : 11837_JOM Dispatch : 28-4-2022 Pages : 10
Article No.: 5317 ☐ LE ☑ CP ☐ TYPESET ☑ DISK

◀Fig. 9. Radial distribution functions for HTIR-Mo and HTIR-Nb for (a–b) DFT and AIMD 20°C and during the AIMD (c–f) heat ramp, (g–h) cool down, and (i–j) subsequent ramp corresponding to the heat up/cool down cycles in Fig. 7. The peaks at 20°C before the heat ramp are numbered for clarity. A version of the heat ramp on a logarithmic scale is provided (e–f) to better discern the structural evolution. Temperatures indicate the constant temperature simulation at which each RDF was obtained. Color coding for the temperatures is consistent across (c)–(j).

that O can also counteract the voltage increase due to P. Like HTIR-Mo, the HTIR-Nb DFT and AIMD 20°C structures are identical (Fig. 9b). Comparing the DFT and AIMD 20°C voltages in Fig. 8b demonstrates that O does decrease the HTIR-Nb voltage slightly. However, greater voltage reductions are observed as the AIMD temperature increases to 1200°C. The better agreement of AIMD-BTE than DFT-BTE with experiment for HTIR-Nb suggests that the DFT-BTE overprediction in voltage is due to the lack of both temperature effect on the structure and O content. Both predictions (3) and (4) are confirmed, though the temperature effect on structure is the larger contributing factor.

The AIMD-BTE voltage predictions are a considerable improvement over the DFT-BTE predictions, with some AIMD structures, notably 600°C, in good agreement with experiment over the full temperature range. It suggests that the atomic structures obtained at 600°C for HTIR-Mo and for HTIR-Nb represent the closest to the average structures of the experimental samples over the full temperature range. This is further supported by the RDFs (Fig. 9). With the exception of HTIR-Nb at 1600°C, the number of peaks and peak intensities is largely converged after 600°C.

Previously, the reduction in voltage of HTIR-TCs during heat treatment was attributed to grain growth.[9] While experiment might have additional structural variations, the RDFs from the AIMD model (Fig. 9) show the extent to which the heat treatment induces change at length scales as small as atom-atom distances.

CONCLUSION

Through a combination of experiment, DFT, BTE, and AIMD, we demonstrated that HTIR-TC performance can be predicted computationally based on composition. The combined AIMD and BTE method is the most effective to predict the HTIR-Mo and HTIR-Nb structures and Seebeck EMFs for the full temperature range. The AIMD structures are converged after 600°C, resulting in the best voltage match to experiment. The La and P additives increase the temperature resolution compared to the pure metals, as seen in the DFT-BTE model. In HTIR-Mo, O increases the voltage with temperature. In HTIR-Nb, O causes a slight reduction in the voltage. Temperature significantly affects the atomic structure, leading to changes in the EMF. In both HTIR-Mo and -Nb, the AIMD voltages change over the duration of the heat ramp despite the additive concentrations remaining constant. The decrease in the output voltage during the experimental heat treatment is correlated with the previous study of grain growth. Our further study also shows that structural changes occur at the atomic scale. Our work can support the investigation of different HTIR-TC materials built towards longer lifetimes. The AIMD-BTE method can be used to study the effects of transmutation of the constituent materials, oxidation, or the onset of other radiation-induced point defects on HTIR-TC performance. Additionally, the performance of TCs consisting of alloyed thermoelements or containing different additives can be predicted. With accurate, durable in-pile temperature sensors, research reactor studies and ATF materials can be better characterized.

ACKNOWLEDGEMENTS

The authors would like to thank Dr. Brian J. Jaques from Boise State University for helpful discussions of this work. This work was supported in part through the Department of Energy Advanced Sensors and Instrumentation program under DOE Idaho Operations Office Contract DE-AC07-05ID14517. The views and opinions of authors expressed herein do not necessarily state or reflect those of the US Government or any agency thereof. Modeling was performed at the High-Performance Computing Center at Idaho National Laboratory, which is supported by the Office of Nuclear Energy of the US Department of Energy and the Nuclear Science User Facilities under Contract No. DE-AC07-05ID14517. Further computational resources were provided by the R2 cluster (https://doi.org/10.18122/B2S41H) provided by Boise State University's Research Computing Department.

CONFLICT OF INTEREST

The authors declare that they have no conflict of interest.

REFERENCES

1. H. Pfister, *Cryogenics* 16, 17 https://doi.org/10.1016/0011-2275(76)90281-2 (1976).
2. P. Kneisel, G. Ciovati, P. Dhakal, K. Saito, W. Singer, X. Singer, and G.R. Myneni, *Nucl. Instruments Methods Phys. Res. Sect. A* 774, 133 https://doi.org/10.1016/j.nima.2014.11.083 (2015).
3. Q.G. Mu, B. Bin Ruan, K. Zhao, B.J. Pan, T. Liu, L. Shan, G.F. Chen, and Z.A. Ren, *Sci. Bull.* 63, 952 https://doi.org/10.1016/j.scib.2018.06.011 (2018).
4. J.L. Rempe, D.L. Knudson, K.G. Condie, and S.C. Wilkins, *Nucl. Technol.* 156, 320 https://doi.org/10.13182/NT06-A3794 (2006).
5. B.G. Kim, J.L. Rempe, J. Villard, and S. Solstad, *Radiat. Meas. Gen. Instrum.* 176, 155 https://doi.org/10.13182/NT11-A13294 (2011).
6. S.J. Zinkle, K.A. Terrani, J.C. Gehin, L.J. Ott, and L.L. Snead, *J. Nucl. Mater.* 448, 374 https://doi.org/10.1016/j.jnucmat.2013.12.005 (2014).

7. J.K. Watkins, A. Gonzales, A.R. Wagner, E.S. Sooby, and B.J. Jaques, *J. Nucl. Mater.* 553, 1 https://doi.org/10.1016/j.jnucmat.2021.153048 (2021).
8. J.L. Rempe, D.L. Knudson, K.G. Condie, J.C. Crepeau, J.E. Daw, and S.C. Wilkins, *Nucl. Technol.* 167, 169 https://doi.org/10.13182/NT09-14 (2009).
9. J. Daw, J. Crepeau, J. Rempe, D. Knudson, K. Condie, and C. Wilkins, *J. Power Energy Syst.* 2, 854 https://doi.org/10.1299/jpes.2.854 (2008).
10. R. Skifton, J. Palmer, and P. Calderoni, *Instrum. Sci. Technol.* 46, 1 https://doi.org/10.1080/10739149.2017.1389754 (2017).
11. R. S. Skifton, J. Palmer, L. Kurt, P. Calderoni, D. Corbett, and E. L. Sikorski, in *11th Nucl. Plant Instrumentation, Control Human-Machine Interface Technol.* (2019).
12. A.J. Palmer, R.S. Skifton, M. Scervini, D.C. Haggard, and W.D. Swank, *EPJ Web Conf. ANIMMA* 2019, 225 https://doi.org/10.1051/epjconf/202022504010 (2020).
13. M. Scervini, C. Rae, and B. Lindley, in *2013 3rd International Conference on Advancements in Nuclear Instrumentation, Measurement Methods Instrumentation, Meas. Methods Their Appl.* (2013) https://doi.org/10.1109/ANIMMA.2013.6727900.
14. A. J. Palmer, D. C. Haggard, J. W. Herter, M. Scervini, W. D. Swank, D. L. Knudson, and R. S. Cherry, in *2015 4th International Conference on Advancements in Nuclear Instrumentation, Measurement Methods Their Applications* (2015) https://doi.org/10.1109/ANIMMA.2015.7465501.
15. G. Kresse, and J. Furthmüller, *Phys. Rev. B* 54, 11169 https://doi.org/10.1103/PhysRevB.54.11169 (1996).
16. J.P. Perdew, K. Burke, and M. Ernzerhof, *Phys. Rev. Lett.* 77, 3865 https://doi.org/10.1103/PhysRevLett.77.3865 (1996).
17. S.L. Dudarev, G.A. Botton, S.Y. Savrasov, Z. Szotek, W.M. Temmerman, and A.P. Sutton, *Phys. Status Solidi* 166, 429 https://doi.org/10.1002/(SICI)1521-396X(199803)166:1%3c429::AID-PSSA429%3e3.0.CO;2-F (1998).
18. S. Lutfalla, V. Shapovalov, and A.T. Bell, *J. Chem. Theory Comput.* 7, 2218 https://doi.org/10.1021/ct200202g (2011).
19. H. Kamisaka, T. Suenaga, H. Nakamura, and K. Yamashita, *J. Phys. Chem. C* 114, 12777 https://doi.org/10.1021/jp104355q (2010).
20. G.K.H. Madsen, J. Carrete, and M.J. Verstraete, *Comput. Phys. Commun.* 231, 140 https://doi.org/10.1016/j.cpc.2018.05.010 (2018).
21. K. Momma, and F. Izumi, *J. Appl. Crystallogr.* 44, 1272 https://doi.org/10.1107/S0021889811038970 (2011).
22. C. Bernuy-Lopez, M. Allix, C.A. Bridges, J.B. Claridge, and M.J. Rosseinsky, *Chem. Mater.* 19, 1035. https://doi.org/10.1021/cm0624116 (2007).
23. A.U. Seybolt, *JOM* 6, 774 https://doi.org/10.1007/BF03377426 (1954).
24. S. Nosé, *J. Chem. Phys.* 46, 511 https://doi.org/10.1063/1.447334 (1984).
25. N. Cusack, and P. Kendall, *Proc. Phys. Soc.* 72, 898 https://doi.org/10.1088/0370-1328/72/5/429 (1958).
26. R. Schley, and G. Metauer, *Temp. Its Meas. Control Sci. Ind.* 5, 1109 (1982).
27. V. Raag, and H.V. Kowger, *J. Appl. Phys.* 36, 2045 https://doi.org/10.1063/1.1714399 (1965).
28. P.-J. Yang, Q.-J. Li, T. Tsuru, S. Ogata, J.-W. Zhang, H.-W. Sheng, Z.-W. Shan, G. Sha, W.-Z. Han, J. Li, and E. Ma, *Acta Mater.* 168, 331 https://doi.org/10.1016/j.actamat.2019.02.030 (2019).